PHYSICAL REVIEW B **87**, 014427 (2013)

Mapping the domain wall pinning profile by stochastic imaging reconstruction

Wanjun Jiang,[1,*] Yabin Fan,[1] Pramey Upadhyaya,[1] Murong Lang,[1] Minsheng Wang,[1] Li-Te Chang,[1] Kin L. Wong,[1]
Jianshi Tang,[1] Mark Lewis,[1] Jing Zhao,[1] Liang He,[1] Xufeng Kou,[1] Caifu Zeng,[1] X. Z. Zhou,[2]
Robert N. Schwartz,[1,†] and Kang L. Wang[1,‡]
[1]*Device Research Laboratory, Electrical Engineering Department, University of California, Los Angeles, California 90095, USA*
[2]*Department of Physics and Astronomy, University of Manitoba, Winnipeg, Manitoba, Canada, R3T 2N2*

(Received 16 July 2012; revised manuscript received 28 November 2012; published 25 January 2013)

Polar magneto-optical Kerr effect microscopy and subsequent stochastic imaging reconstruction have been used to map out the distinct pinning profiles of randomly distributed intrinsic defects (pointlike/linelike), as well as their dependence on the external magnetic field in 2-μm-thick yttrium iron garnet films. A comparison of the pinning profiles produced by these intrinsic defects and the extrinsic defects (made by focused ion beam lithography) has also been made. In addition, we have found a linear dependence of the pinning potentials on the depths of the fabricated pointlike defects. Our observations should provide a fundamental understanding of the role of defects in domain wall spintronics.

DOI: 10.1103/PhysRevB.87.014427 PACS number(s): 75.60.Ch, 75.50.Gg, 75.70.Kw

I. INTRODUCTION

The natural formation of magnetic domains and domain walls (DWs) in the macroscopic magnetic materials relies on the complex, as well as competing interplay between various energy origins: exchange, anisotropy, magnetostatic, and pinning potential.[1–4] Among them, pinning potentials produced by crystalline defects and local structural disorder can be effectively tailored such that DWs move controllably between different attractive pinning sites to implement logic functions and reconfigurable memories.[5–7] A comprehensive understanding of their detailed functionalities is, however, still lacking. In particular, how to characterize the randomly distributed pinning sites, the resultant pinning potential profiles, as well as their dependences on the external magnetic fields, are questions that remain to be resolved.

Here we apply a stochastic imaging reconstruction (SIR) technique to process polar magneto-optical Kerr effect (MOKE) microscopy data to successfully map out both intrinsic and extrinsic randomly distributed defects (pointlike/linelike) and their distinct pinning profiles in a macroscopic system. Our observations should provide a fundamental understanding of the role of defects in DW engineering, which can be extended to a variety of complex systems with disorder driven dynamics, such as ferroelectric DW dynamics[8] and superconducting vortex dynamics.[9]

It is well known that magnetic DWs can be pinned by structural defects in magnetic materials.[10] These defects can be intrinsic (naturally occurring) and extrinsic (artificially introduced) and produce an attractive pinning potential ($U(r)$), which in turn enable DWs to sit in local energy minima and consequently modify the position, shape, and direction of propagation of DWs, as well as the local magnetization dynamics.[1–4] Control of spin dynamics in nanoscale systems via artificial structural defects has been demonstrated in magnetic nanowires.[11–16]

While the underlying cause of DW pinning by crystalline defects has been known for nearly a century as the Barkhausen effect,[1–4] the direct experimental evaluation of the potential profiles created by the randomly distributed and magnetically active pinning sites in macroscopic system is currently a great challenge.[17–27] Note that conventional structural characterization tools offer a direct measure of the presence of various defects; however, their experimental links to the pinning potential remained elusive. This stems from the competitive interactions that lead to the stochastic pinning/depinning of DWs, which is a manifestation of the system's complex energy landscape with an infinite number of metastable states.[25–27] The previous stochastic elements, however, have not been comprehensively addressed in earlier experimental efforts in which single shot measurements were dominant.[17–24] Consequently, accurate decoding of the potential profile from these *seemingly random* domain configurations was not possible.

II. SAMPLE FABRICATION AND INSTRUMENT

The magnetic systems studied here are 2-μm-thick yttrium iron garnet (YIG) films of composition $(\text{YSmLuCa})_3(\text{FeGe})_5\text{O}_{12}$, grown by liquid phase epitaxial techniques on (111) orientated $\text{Gd}_3\text{Ga}_5\text{O}_{12}$ (GGG) garnet substrates. Due to the preferential ordering of the rare earth ions in the dodecahedral garnet lattice (growth mechanism) as well as the mismatch between the lattice spacing of the film and the substrate (stress mechanism), the YIG film typically exhibits a uniaxial anisotropy with the easy axis perpendicular to the film plane, which has proved to be pivotal for magnetic bubble devices.[2] Well-defined perpendicular anisotropy of our specimen was confirmed by both longitudinal and polar MOKE magnetometry measurements, as well as by direct magnetization measurement using a superconducting quantum interference device (SQUID) magnetometer. DW dynamics were monitored using a polar MOKE imaging system with an optical resolution approaching 360 nm, which was constructed from a commercial Carl Zeiss AxioScope microscope.

Artificial defects were introduced into our YIG film by using focused ion beam (FIB) lithography with a resolution approaching 10 nm (NOVA 600 SEM/FIB system). During ion milling, the acceleration voltage was set at 30 kV, and the ion beam current at 0.1 nA. Due to the high resistivity of the YIG specimen, we have deposited a 150-nm-thick Cr-metallic layer on the surface, which served as a discharging layer that

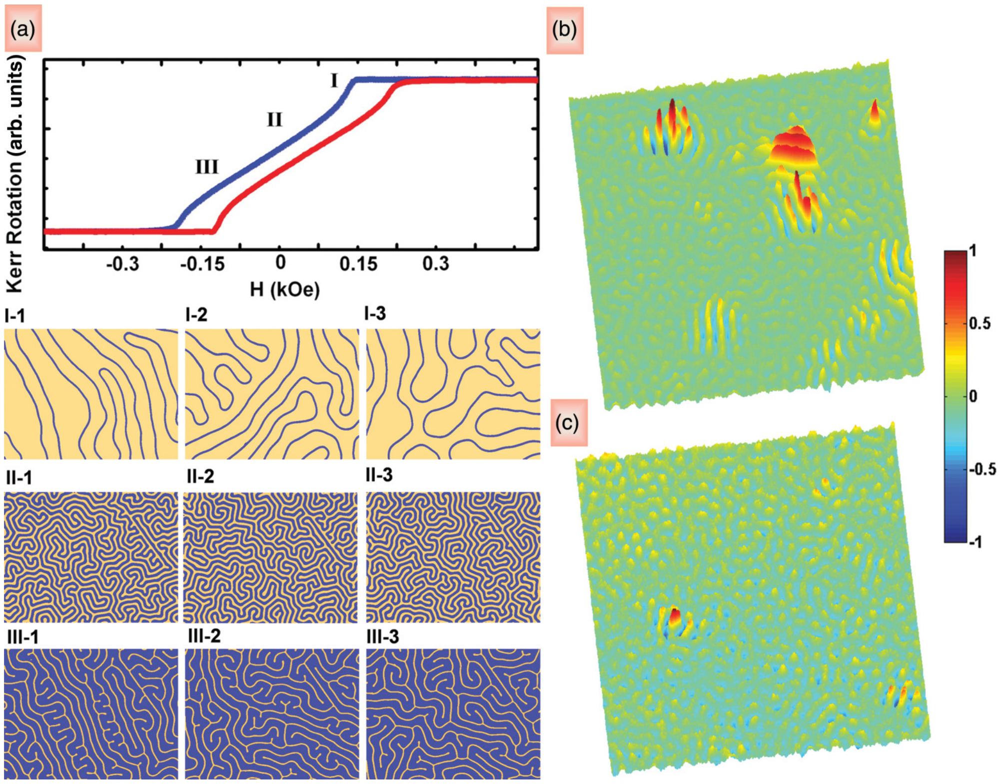

FIG. 1. (Color online) Stochastic DW pinning and the resultant DW pinning profiles. (a) Images of the stochastic DW pinning along the hysteresis loop in a YIG thin film. Specifically, the onset of stochastic DW pinning is observed by performing the repetitive domain imaging experiments (up to 300 times) along the hysteresis loop. For the predetermined fields marked as I, II, and III, one clearly notices the domain configurations acquired under the same condition are different from each other. The onset of stochastic DW nucleation are marked as I-1, I-2, and I-3 from regime I; II-1, II-2, and II-3 from regime II; and III-1, III-2, and III-3 from regime III. (b), (c) Mapping the DW pinning profiles via applying SIR. For varying spatial locations (within imaging area of 120 × 120 μm^2) of YIG thin film, the DW pinning profiles for the intrinsic pointlike defects are dramatically different (at external magnetic field $H = 0$). The color bar is defined between $+1$ and -1, which represent the probability of magnetization being up and down, respectively.

was removed after FIB lithography. To precisely control the depth of these defects, several practice runs were performed to evaluate the related cutting rate, as confirmed by a cross-sectional scanning electron microscope (SEM) image.

III. EXPERIMENTAL RESULTS AND DISCUSSION

Random domain configurations are displayed in Fig. 1(a), which were acquired under identical external parameters, i.e., saturate the system in a magnetic field (H) at 300 Oe and subsequently decrease to various constant fields following the same sweeping rate. This procedure at each field was repeated over 300 times, and the acquired images are given in the supplementary material.[28] From Fig. 1(a), it is straightforward to realize that under the same external conditions the domain configurations acquired differ from each other, which directly reveal the stochastic nature of DW pinning. As a result, this manifold of metastable states hinders the accurate identification of both the location of active pinning sites and the profile of the pinning potentials $U(r, H)$ in the present millimeter scale system.

While the locations of defects are determined, their potential strengths/profiles are difficult to experimentally evaluate in the presence of competitive interactions. The pinning probability $P(r_0, H)$ of DWs at a specific position r_0, however, is directly proportional to both the strength and the profile of a potential well $U(r_0, H)$. In other words, the stronger the potential well, the larger the probability of DWs being trapped. One notes that DWs are not necessarily being pinned at the same location in the repeated experiments, which is also suggested in studies of ferromagnetic nanowires with artificial notches using x-ray transmission microscopy,[12] as well as in the large scale Co thin films using MOKE microscopy.[29,30] Following this rationale, it is then possible to experimentally probe the potential profile of any magnetically active defect via performing statistics on the measurable pinning probability of DWs acquired from the irregularly evolving domain configurations.

In the following, we develop a technique referred to as SIR to map out the DW pinning probability and hence the pining profiles/strengths of dynamically evolving configurations. The collected gray-scale polar MOKE raw images were initially subjected to digital processing and eventually binarized to black/white colors. To be consistent with the direction of the external magnetic field, white color is assigned to the domains with the up (↑) orientation, and the black color is given to the domains with the down (↓) orientation. Without any selective operation, these binarized images were stochastically added together to probe the accumulation of the pinning probability profiles, which were then normalized by the total number of frames sampled. In order to avoid possible erratic variations in the collected images, a random sampling survey is also conducted by carrying out SIR with varying numbers of images, starting from 150 to 500 in steps of 50. As given in the supplementary material (Fig. S6),[28] the establishment of well-defined potential profiles is independent of the number of images sampled, which in turn validates our SIR approach. It is worth mentioning that our SIR method is different when compared with the technique employed for stochastic optical reconstruction microscopy (STORM), which is used to resolve the 3D morphology of stationary nanoscopic cellular structures,[31] not dynamically evolving events such as DW pinning.

As expected, the spatial variation of the pinning probabilities builds up in this macroscopic system ($120 \times 120\ \mu\text{m}^2$) immediately after performing SIR, evident in Figs. 1(b) and 1(c) (the data presented here are acquired at $H = 0$ (regime II) with a constant sweep rate $dH/dt = 8$ Oe/s). Depending on the specific types of underlying defects (intrinsic), such as point defects (the definition of these intrinsic defects are given in the supplementary material, Fig. S4[28]), the potential profiles vary in a consistent manner. The physical origin of these defects cannot be clearly resolved by using a MOKE microscope; however, due to the high quality of liquid phase epitaxial technique, gain boundaries can be reasonably excluded. Stimulated by the extensive discussion of doped semiconductors we believe that in our YIG films pointlike defects can be identified with impurities and vacancies, whereas linelike defects are associated with dislocations.

By characterizing the shapes of these potentials, it is then possible to mathematically define their corresponding profiles. For example, in the case of an intrinsic pointlike defect, the potential profile follows closely a symmetric Gaussian probability function.[2,3,26] A detailed mathematical formulation will be addressed later. In contrast, the potential profile of an intrinsic linelike defect is highly asymmetric (in the x-y plane). Regarding the strengths of the potential wells, given that their values can be found by comparing their pinning probabilities, their absolute amplitudes cannot be obtained by simply following this procedure. The pinning potential profile depends on the material parameters and the exchange (E_E), anisotropy (E_A), and magnetostatic energies

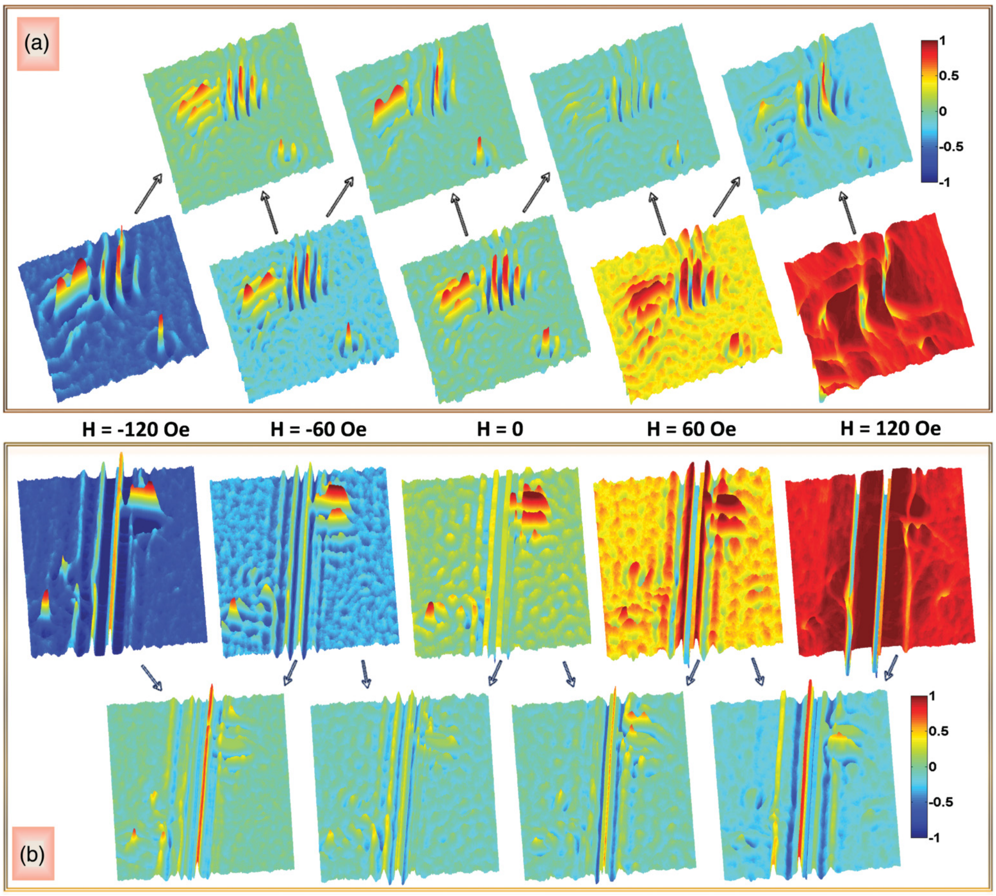

FIG. 2. (Color online) Evolution of the pinning profiles of intrinsic defects with external magnetic fields. After progressively increasing the magnitude of the external magnetic field, the characteristically different pinning profiles of various intrinsic defects in the selected areas ($60 \times 60\ \mu\text{m}^2$) are resolved. For example, for both intrinsic pointlike and linelike defects shown in (a) and (b), by increasing the external magnetic field (from -120 Oe to $+120$ Oe), these profiles are gradually suppressed. In order to address these reductions, subtraction of the adjacent profiles displayed in the upper part of (a) and lower part of (b) are subsequently performed. Based on the subtractions [$(-120\text{ Oe}) - (-60\text{ Oe}), (-60\text{ Oe}) - (0), (0) - (60\text{ Oe})$, and $(60\text{ Oe}) - (120\text{ Oe})$], it is then possible to qualitatively probe the contribution arising from the external magnetic field.

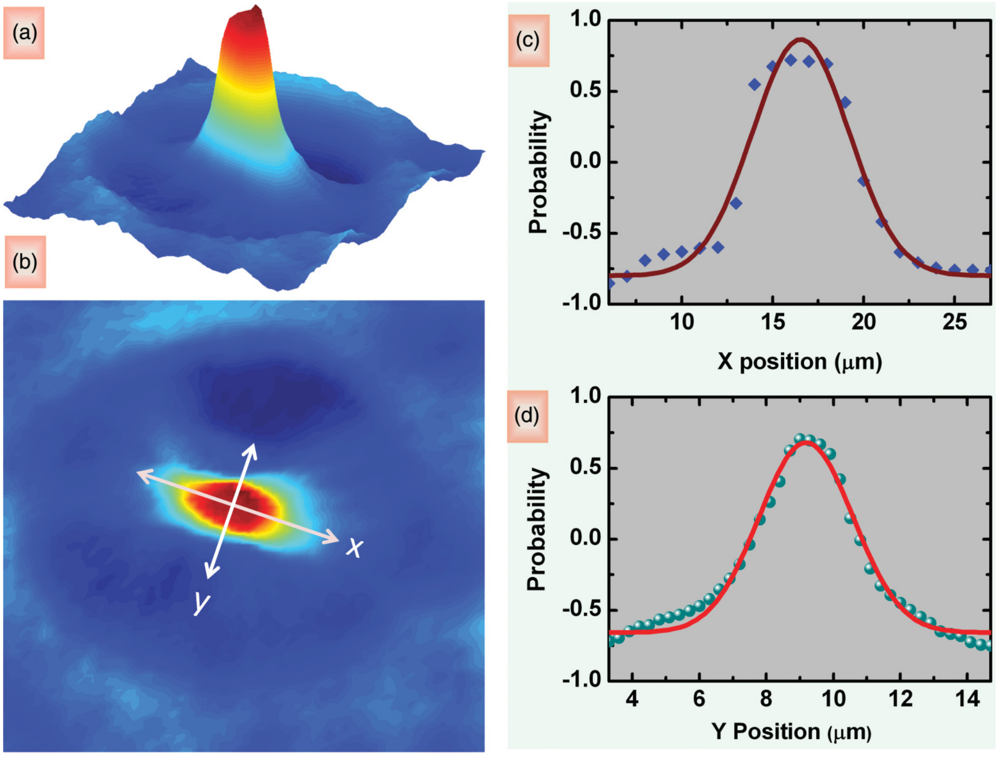

FIG. 3. (Color online) Mathematical characterization of the pinning profile of an intrinsic pointlike defect. Here the pointlike defect is selected from the pinning potential of $H = -120$ Oe, Fig. 2(a) in the main text, and the lower right-hand side corner, which is also circled in Fig. S4 (a) in the supplementary information (Ref. 28). Specifically, a Gaussian function fitting is made along the two slices cutting along the x (c) and the y (d) axes. The good agreement between the mathematical model and the experimental data validates that the pinning profile of pointlike defect can be described by a simple Gaussian function.

(E_M), and its amplitude is difficult to be experimentally estimated.

As discussed previously, the appearance of random domain configurations has its origin in the underlying competitive energy terms. Therefore, it is natural to investigate the evolution of the pinning potential as a function of the external magnetic field strengths. In order to fully address this issue as well as to quantify the strengths of the pinning potentials, measurements at various magnetic fields were subsequently carried out. The resulting pining profiles of different types of defects are shown in Fig. 2 as a function of the externally applied magnetic field (120 Oe, 60 Oe, 0, -60 Oe, and -120 Oe). For the pointlike defects presented in Figs. 2(a) and 2(b), mathematical subtraction of the adjacent potential profiles is also performed, which enables a qualitative characterization of the spatial variation/distortion of the potential difference induced by the external magnetic field, as shown in Figs. 3(c) and 3(d) along the x and y axes, respectively. It is noted that a mathematic model of the intrinsic linelike defects is highly challenging due to the asymmetric pinning profiles in the x-y directions.

For the purpose of making a direct comparison of the pinning profiles associated with intrinsic and extrinsic defects, extrinsic defects were created by employing FIB lithography. An artificially introduced ringlike defect with an outer diameter $R_1 = 20$ μm, an inner diameter $R_2 = 19.85$ μm, and depth $D = 200$ nm is shown in Fig. 4(a). Figure 4(b) was obtained by using a SEM in the cross-sectional mode. In order to reveal the stochastic nucleation of DWs around the extrinsic ring defect, MOKE imaging data displayed in Figs. 4(c)–4(g) are shown with the superimposed conventional optical image. Based on the sequence of images given below, one realizes that while the pinning events look random, the pinning probability around the artificial ring defect is clearly larger than in the area without a pinning site. This occurs as a result of the artificially created pinning potential that modifies the energy landscape and hence the related magnetization dynamics.

In order to quantify the local stochastic magnetization dynamics (70×70 μm^2) that occurred around the aforementioned artificial ring defect, the magnetization deviation (ΔM) is estimated by calculating the differences between the white (magnetization with up orientation, $M_\uparrow$) and black (magnetization with down orientation, $M_\downarrow$) regions, and is shown in Fig. 4(h). Such data with irregular jumps is a manifestation of the occurrence of varying magnetization (M) during the repetitive experiments, which offers a direct measure of the stochastic magnetization dynamics resulting from the competition between the various contributions to the magnetic energy.

After performing SIR, the pinning potentials are revealed, as shown in Figs. 4(i)–4(k). The formation of several periodically concentric rings around the artificial ring defect, at $H = 0$ in particular, is observed. Such interesting behavior arises from the strong magnetostatic confining potential created by the ring defect. Indeed, when an external magnetic field is applied, one clearly observes that these seemingly "quantized" patterns are eliminated, as with fields $H = -120$ Oe and 120 Oe,

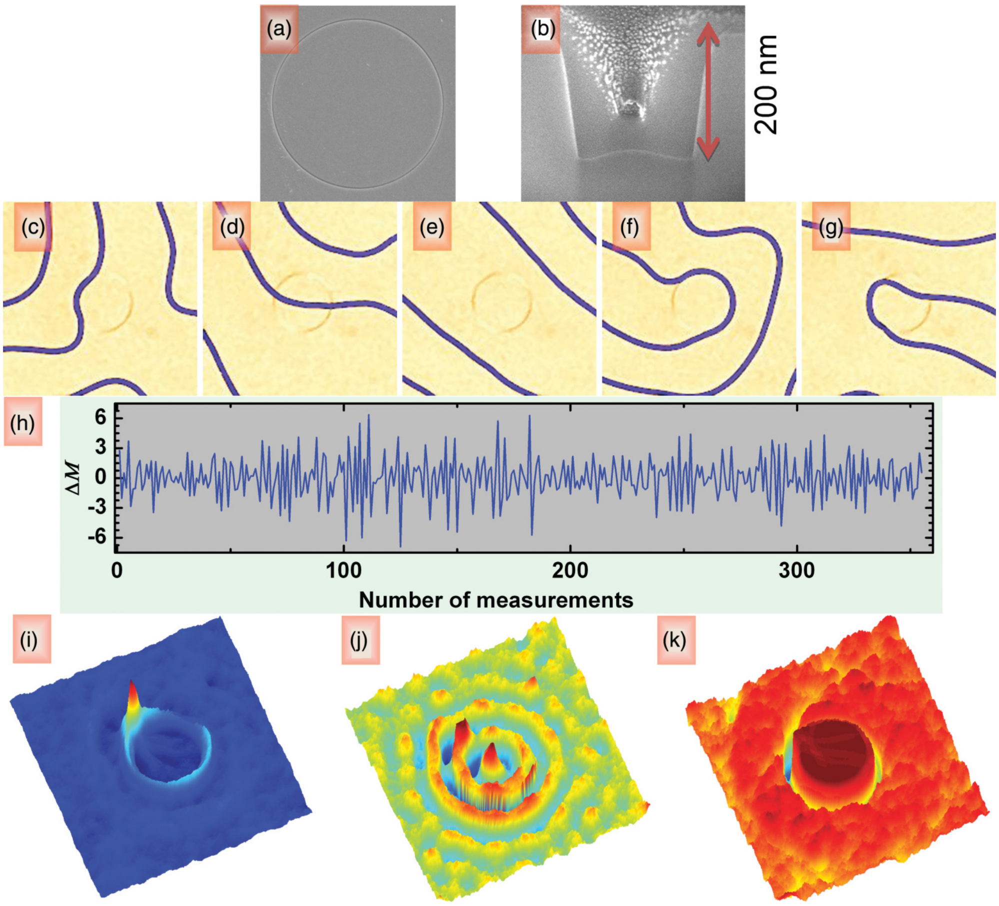

FIG. 4. (Color online) Stochastic domain pinning around the extrinsically introduced ring defects. This type of artificial defect is introduced by using FIB lithography, where the outer diameter is 20 μm and inner diameter is 19.8 μm, as shown in (a) and the depth ($D = 200$ nm) as given in (b). The stochastic DW pinning in the presence of an artificially introduced ring defect is revealed in (c)–(g). The images are combinations of MOKE (at $H = 120$ Oe) and conventional optical images, which enable a better presentation of the stochastic DW pinning around the ring defect. A quantification of the local stochastic magnetization dynamics around the ring defect is offered in (h) by calculating the magnetization (M) from the area difference between magnetization with up and down orientations, from which one clearly observes the irregular jumps. Here $\Delta M = M - \overline{M}$ represents the deviation from the average magnetization. From the consecutive images acquired at $H = -120$ Oe (i), $H = 0$ (j), and $H = 120$ Oe (k), it is straightforward to realize that the pinning profiles established from the SIR approach are gradually suppressed by the external magnetic field as a consequence of the increasing Zeeman energy contribution. Note that the point with enhanced pinning probability is due to the overlap between the initial and final cutting during FIB lithography.

respectively. Nevertheless, a comprehensive understanding on these pattern formations inside the ring defect (while not the primary focus of the present study) can be established by performing further intensive experiments on the ring defects with various diameters.

In the multidomain case, the magnetic field-dependent effective potential barrier can be quantitatively expressed as $U(r, H) = U_0(r)(1 - H/H_0)^{\alpha}$.[22,26] Here U_0 is the amplitude of the barrier at zero magnetic field, and H_0 is the temperature-dependent characteristic critical field that measures the competition between the Zeeman energy and the pinning potential energy. Namely, when $H > H_0$, the Zeeman energy dominates, whereas when $H < H_0$, the pinning potential is dominant. The universal exponent α is related to the roughness exponent of a disordered system,[22,26] for example, $\alpha = 3/2$ for the macroscopic system when the thermal fluctuations can be considered perturbatively, i.e., $U(r, H) \gg k_B T$.[27,32] Subsequently, with access to the measurable pinning probability $P(r_0, H)$, the escaping probability $E(r_0, H)$ from a potential barrier can be defined as $1 - P(r_0, H)$, which can be empirically determined by an Arrenhius-Néel-type relation as follows:[27,33,34]

$$E(r_0, H) = \exp\left(-\frac{U_0}{k_B T} \cdot |H/H_0|^{\alpha}\right), \qquad (1)$$

where T is the measurement temperature (300 K), and k_B is the Boltzmann constant. Using these facts, the parameters for the potential barriers can be determined by exponentially fitting the pinning probability as a function of applied field; the results are shown in Fig. 5(a). For the point defect, these parameters are $U_0 \approx 0.26\,\text{eV} \approx 10\,k_B T$ (directly validating the aforementioned model), $H_0 \approx 128$ Oe, and exponent $\alpha \approx 3/2$. Summarized in Table I are the pertinent parameters determined from the fit. However, the potential barriers $U_0 \approx 0.13\,\text{eV} \approx 5\,k_B T$ determined from the previous Arrenhius model for the line effect are not strictly satisfying the

TABLE I. Fitted parameters of the pinning potential profiles. From Eq. (1), and following the procedure described in the main text as well as supplementary material (Ref. 28), all parameters can be self-consistently determined by using a natural logarithmic fitting procedure. For example, U_0 is determined by simply calculating the value of $k_B T \cdot ln[E(r_0, 0)]$; H_0 and α are acquired by fitting Eq. (1).

	U_0 (eV)	H_0 (Oe)	Exponent (α)
Point defect_1	0.38	128 ± 1	1.40 ± 0.05
Point defect_2	0.30	114 ± 1	1.35 ± 0.05
Line defect_1	0.11	117 ± 1	1.60 ± 0.05
Line defect_2	0.17	121 ± 1	1.55 ± 0.05
Ring defect	0.31	124 ± 1	1.45 ± 0.05

approximation of $U(r, H) \gg k_B T$. While the exact origin of this phenomenon is not clear yet, it might arise from the increased DW elastic energy with a significant reduction of both DW roughness and speed, as suggested in ultrathin Pt/Co/Pt films with line defects.[7,19] Indeed, recent theoretical calculations have demonstrated that the energy barrier decreases as the defect size increases.[35] Comparing recent results on the determination of both the potential strength and the profile obtained from microwave power spectrum measurements in a permalloy nanostructure,[36] it is clear that our method offers a direct way of quantifying the strength and the profile, as well as the distortion of pinning potentials modified by an additional Zeeman magnetostatic energy term.

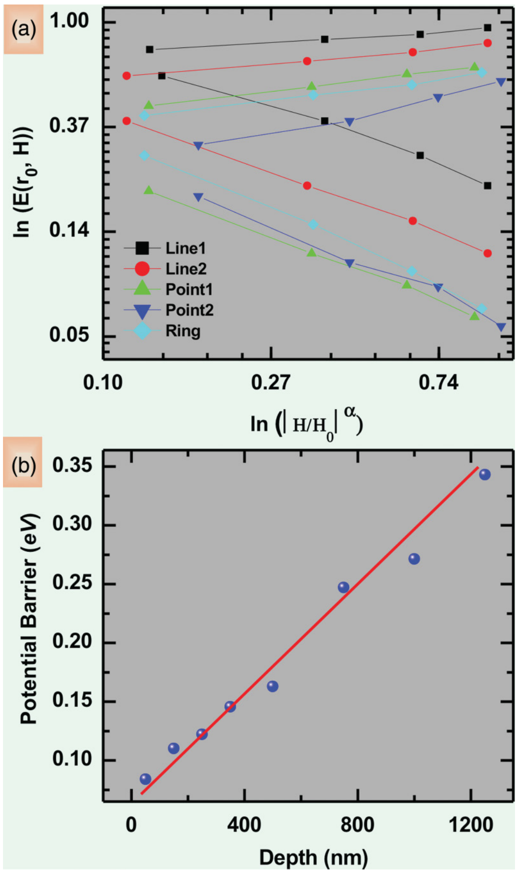

FIG. 5. (Color online) The experimental determination of the associated parameters for the potential profiles. Based on the acquired field-dependent pinning probability $P(r_0, H)$, the escaping probability $E(r_0, H)$ is calculated as $1 - P(r_0, H)$. Subsequently, a $ln - ln$ fitting of $E(r_0, H)$ vs. $|H/H_0|$ enables the remaining parameters H_0 and α to be consistently determined, as tabulated in the Table I. (b) Correlation between the depth and the pinning potential of the artificially introduced pointlike defects. This correlation can be closely quantified by a linear function that enables the local DW pinning/depinning dynamics to be precisely correlated with the crystalline pinning centers.

It is noted that our experiment is different from conventional time-dependent relaxation-like measurements in which the switching probability is defined as $P \propto e^{-t/\tau}$.[27] Indeed, prior to recording MOKE imaging data for SIR, we stayed for more than 15 seconds at the predetermined magnetic fields in order to achieve stabilization. This is important for the purpose of eliminating magnetic domain relaxation that is typically associated with the magnetic after-effect. The absence of domain relaxation after this time scale is confirmed by performing time-dependent MOKE imaging, which validates the motivation of employing the time-independent Arrenhius-Néel-type relation.

Returning to the artificial defects, the amplitudes of their pinning potentials can also be determined based on the previous approach, which subsequently enables the correlation between the depths of these defects and the amplitudes of their resultant pinning potentials to be constructed. Figure 5(b) clearly shows the linear dependence of the pinning potentials on the depths of the fabricated pointlike defects. More importantly, such a linear correlation suggests that with access to the proper characterization of the pinning potentials created by the crystalline defects, it is possible to control the associated DW (pinning/depinning) dynamics in the corresponding systems (the universality class of DW motion[17,28] is a representative example of this correlation).

IV. SUMMARY

In summary, by employing polar MOKE imaging, we have revealed the stochastic nature of DW nucleation, and via the proposed approach, SIR, we have successfully mapped the spatial variation of DW pinning profiles induced by various types of defects (point and line) in macroscopic YIG films. A direct comparison is made by introducing artificial defects via FIB lithography. Our approach provides a fundamentally important route to quantify the strengths of intrinsic/extrinsic structural defects, which could expedite DW engineering for the realization of a variety of vital spintronics applications.

ACKNOWLEDGMENTS

Financial support from the Focus Center Research Program-Center on Functional Engineered Nano Architectonics (FENA), the Western Institute of Nanoelectronics (WIN), and the Defense Advanced Research Projects Agency (DARPA) is appreciated. We also thank the technical support from Noah Bodzin at UCLA for the access to a Nova 600 SEM/FIB system. The authors acknowledge insightful comments made by Dr. Peter Fisher.

[*] wjiang@ee.ucla.edu
[†] rns@ee.ucla.edu
[‡] wang@ee.ucla.edu

[1] A. Morrish, *The Physical Principles of Magnetism* (IEEE Press, New York, 1965).

[2] A. P. Malozemoff and J. C. Slonczewski, *Magnetic Domain Walls in Bubble Materials* (Academic Press, New York, 1979).

[3] A. Hubert and R. Schafer, *Magnetic Domains: The Analysis of Magnetic Microstructures* (Springer, Berlin, Heidelberg, New York, 2008).

[4] C. H. Marrows, Adv. Phys. **54**, 585 (2005).

[5] D. A. Allwood, G. Xiong, C. C. Faulkner, D. Atkinson, D. Petit, and R. P. Cowburn, Science **309**, 1688 (2005).

[6] S. S. P. Parkin, M. Hayashi, and Luc. Thomas, Science **320**, 190 (2008).

[7] L. Krusin-Elbaum, T. Shibauchi, B. Argyle, L. Gignac, and D. Weller, Nature **410**, 444 (2001).

[8] S. Jesse, B. J. Rodriguez, S. Choudhury, A. P. Baddorf, I. Vrejoiu, D. Hesse, M. Alexe, E. A. Eliseev, A. N. Morozovska, J. Zhang, L. Q. Chen, and S. V. Kalinin, Nat. Mater. **7**, 209 (2008).

[9] G. Blatter, M. V. Feigel'Man, V. B. Geshkenbein, A. I. Larkin, and V. M. Vinokur, Rev. Mod. Phys. **66**, 1125 (1994).

[10] J. M. D. Coey, *Magnetism and Magnetic Materials* (Cambridge University Press, Cambridge, 2010).

[11] A. Yamaguchi, T. Ono, S. Nasu, K. Miyake, K. Mibu, and T. Shinjo, Phys. Rev. Lett. **92**, 077205 (2004).

[12] Mi-Young Im, L. Bocklage, P. Fischer, and G. Meier, Phys. Rev. Lett. **102**, 147204 (2009).

[13] S. Lepadatu, A. Vanhaverbeke, D. Atkinson, R. Allenspach, and C. H. Marrows, Phys. Rev. Lett. **102**, 127203 (2009).

[14] S. Lepadatu and Y. B. Xu, Phys. Rev. Lett. **92**, 127201 (2004).

[15] D. Petit, A. V. Jausovec, H. T. Zeng, E. Lewis, L. O'Brien, D. Read, and R. P. Cowburn, Phys. Rev. B **79**, 214405 (2009).

[16] L. K. Bogart, D. Atkinson, K. O'Shea, D. McGrouther, and S. McVitie, Phys. Rev. B **79**, 054414 (2009).

[17] M. Yamanouchi, J. Ieda, F. Matsukura, S. E. Barnes, S. Maekawa, and H. Ohno, Science **317**, 1726 (2007).

[18] M. Seul, L. R. Monar, L. O'gorman, and R. Wolfe, Science **254**, 1616 (1991).

[19] T. Shibauchi, L. Krusin-Elbaum, V. M. Vinokur, B. Argyle, D. Weller, and B. D. Terris, Phys. Rev. Lett. **87**, 267201 (2001).

[20] J. P. Attané, Y. Samson, A. Marty, J. C. Toussaint, G. Dubois, A. Mougin, and J. P. Jamet, Phys. Rev. Lett. **93**, 257203 (2004).

[21] P. Haibach, M. Huth, and H. Adrian, Phys. Rev. Lett. **84**, 1312 (2000).

[22] S. Lemerle, J. Ferré, C. Chappert, V. Mathet, T. Giamarchi, and P. Le Doussal, Phys. Rev. Lett. **80**, 849 (1998).

[23] M. Muñoz and José L. Prieto, Nature Commun. **2**, 562 (2011).

[24] R. H. Koch, G. Grinstein, G. A. Keefe, Y. Lu, P. L. Trouilloud, W. J. Gallagher, and S. S. P. Parkin, Phys. Rev. Lett. **84**, 5419 (2000).

[25] J. Akerman, M. Muñoz, M. Maicas, and J. L. Prieto, Phys. Rev. B **82**, 064426 (2010).

[26] P. Chauve, T. Giamarchi, and P. Le Doussal, Phys. Rev. B **62**, 6241 (2000); M. V. Feigel'man, V. B. Geshkenbein, A. I. Larkin, and V. M. Vinokur, Phys. Rev. Lett. **63**, 2303 (1989).

[27] W. Wernsdorfer, E. B. Orozco, K. Hasselbach, A. Benoit, B. Barbara, N. Demoncy, A. Loiseau, H. Pascard, and D. Mailly, Phys. Rev. Lett. **78**, 1791 (1997).

[28] See Supplemental Material at http://link.aps.org/supplemental/10.1103/PhysRevB.87.014427 for imaging processing technique, definition of defects, random sampling survey, pinning profiles created by both intrinsic and extrinsic defect, and MOKE raw data.

[29] D.-H. Kim, S.-B. Choe, and S.-C. Shin, Phys. Rev. Lett. **90**, 087203 (2003).

[30] M.-Y. Im, S.-H. Lee, D.-H. Kim, P. Fischer, and S.-C. Shin, Phys. Rev. Lett. **100**, 167204 (2008).

[31] B. Huang, W. Wang, M. Bates, and X. W. Zhuang, Science **319**, 810 (2008).

[32] R. H. Victora, Phys. Rev. Lett. **63**, 457 (1989).

[33] L. O'Brien, D. Petit, E. R. Lewis, R. P. Cowburn, D. E. Read, J. Sampaio, H. T. Zeng, and A. V. Jausovec, Phys. Rev. Lett. **106**, 087204 (2011).

[34] J. P. Attané, D. Ravelosona, A. Marty, Y. Samson, and C. Chappert, Phys. Rev. Lett. **96**, 147204 (2006).

[35] Yuejin Zhu, Xian Yu, and Shufeng Zhang, Phys. Rev. B **78**, 144411 (2008).

[36] D. Bedau, M. Kläui, M. T. Hua, S. Krzyk, U. Rüdiger, G. Faini, and L. Vila, Phys. Rev. Lett. **101**, 256602 (2008).